

## Adaptive optics enables multimode 3D super-resolution microscopy via remote focusing

Navikas, Vytautas; Descloux, Adrien C.; Grussmayer, Kristin S.; Marion, Sanjin; Radenovic, Aleksandra

**DOI**

[10.1515/nanoph-2021-0108](https://doi.org/10.1515/nanoph-2021-0108)

**Publication date**

2021

**Published in**

Nanophotonics

**Citation (APA)**

Navikas, V., Descloux, A. C., Grussmayer, K. S., Marion, S., & Radenovic, A. (2021). Adaptive optics enables multimode 3D super-resolution microscopy via remote focusing. *Nanophotonics*, *10*(9), 2451-2458. <https://doi.org/10.1515/nanoph-2021-0108>

**Important note**

To cite this publication, please use the final published version (if applicable). Please check the document version above.

**Copyright**

Other than for strictly personal use, it is not permitted to download, forward or distribute the text or part of it, without the consent of the author(s) and/or copyright holder(s), unless the work is under an open content license such as Creative Commons.

**Takedown policy**

Please contact us and provide details if you believe this document breaches copyrights. We will remove access to the work immediately and investigate your claim.



## Research article

Vytautas Navikas, Adrien C. Descloux, Kristin S. Grussmayer, Sanjin Marion and Aleksandra Radenovic\*

# Adaptive optics enables multimode 3D super-resolution microscopy via remote focusing

<https://doi.org/10.1515/nanoph-2021-0108>

Received March 12, 2021; accepted May 20, 2021;

published online June 10, 2021

**Abstract:** A variety of modern super-resolution microscopy methods provide researchers with previously inconceivable biological sample imaging opportunities at a molecular resolution. All of these techniques excel at imaging samples that are close to the coverslip, however imaging at large depths remains a challenge due to aberrations caused by the sample, diminishing the resolution of the microscope. Originating in astro-imaging, the adaptive optics (AO) approach for wavefront shaping using a deformable mirror is gaining momentum in modern microscopy as a convenient approach for wavefront control. AO has the ability not only to correct aberrations but also enables engineering of the PSF shape, allowing localization of the emitter axial position over several microns. In this study, we demonstrate remote focusing as another AO benefit for super-resolution microscopy. We show the ability to record volumetric data ( $45 \times 45 \times 10 \mu\text{m}$ ), while keeping the sample axially stabilized using a standard

widefield setup with an adaptive optics addon. We processed the data with single-molecule localization routines and/or computed spatiotemporal correlations, demonstrating subdiffraction resolution.

**Keywords:** adaptive optics; astigmatism-based single molecule localization microscopy; 3D imaging; remote focusing; single-molecule localization microscopy (SMLM); super-resolution optical fluctuation imaging (SOFI).

## 1 Introduction

Conventional light microscopy methods are inherently constrained in terms of their lateral and axial resolution due to the limited numerical aperture of the imaging apparatus and the finite wavelength of the fluorescence. During the past two decades, multiple approaches were developed to overcome this restriction by exploiting spatial and/or temporal separation of fluorescent emitters [1]. In single-molecule localization microscopy (SMLM) the diffraction limit is circumvented by computationally fitting the point-spread function (PSF) of temporally separated single emitters. SMLM analysis requires a long sequence of sparsely blinking fluorophores in order to appropriately sample the labeled structure. This sequence is typically acquired with high illumination intensities and by using complex imaging buffers with oxygen scavenging systems [2] to minimize the bleaching or by using genetically encoded photo-switchable proteins [3]. To speed up the acquisition procedure and perform imaging in varying fluorophore density environments, alternative computational approaches were developed [4, 5]. For example, Super-resolution Optical Fluctuation Imaging (SOFI) relies on spatiotemporal correlations of the signal of independently blinking emitters. SOFI is particularly suitable to imaging samples with higher fluorophore densities and is less sensitive to varying blinking conditions [6]. Both single-molecule localization methods and SOFI are not restricted to 2D imaging. However, obtaining an axial resolution beyond the diffraction limit throughout the full

\*Corresponding author: **Aleksandra Radenovic**, Laboratory of Nanoscale Biology, Institute of Bioengineering, School of Engineering, Swiss Federal Institute of Technology Lausanne (EPFL), Lausanne, Switzerland, E-mail: [aleksandra.radenovic@epfl.ch](mailto:aleksandra.radenovic@epfl.ch), <https://orcid.org/0000-0001-8194-2785>

**Vytautas Navikas, Adrien C. Descloux and Sanjin Marion**, Laboratory of Nanoscale Biology, Institute of Bioengineering, School of Engineering, Swiss Federal Institute of Technology Lausanne (EPFL), Lausanne, Switzerland, E-mail: [vytautas.navikas@epfl.ch](mailto:vytautas.navikas@epfl.ch) (V. Navikas), [adrien.descloux@epfl.ch](mailto:adrien.descloux@epfl.ch) (A.C. Descloux), [sanjin.marion@epfl.ch](mailto:sanjin.marion@epfl.ch) (S. Marion). <https://orcid.org/0000-0002-2730-0527> (V. Navikas). <https://orcid.org/0000-0002-3101-6641> (A.C. Descloux). <https://orcid.org/0000-0002-9892-7378> (S. Marion)

**Kristin S. Grussmayer**, Laboratory of Nanoscale Biology, Institute of Bioengineering, School of Engineering, Swiss Federal Institute of Technology Lausanne (EPFL), Lausanne, Switzerland; and Grussmayer Lab, Department of Bionanoscience, Faculty of Applied Science, Kavli Institute for Nanoscience Delft, Delft University of Technology, Delft, Netherlands, E-mail: [K.S.Grussmayer@tudelft.nl](mailto:K.S.Grussmayer@tudelft.nl). <https://orcid.org/0000-0003-4515-4356>

thickness of adherent cells (4–10  $\mu\text{m}$ ) is not usually achieved and requires a modified detection path [7].

In SMLM, one of the first and most common ways to retrieve information of the axial PSF position is the introduction of astigmatism in the detection path by using a cylindrical lens [8] or a wave-front shaping optical element such as a deformable mirror [9]. Complex PSF engineering techniques such as the Zernike optimized localization approach [10] allows the adjustment of the PSF for the extended  $Z$ -range (2–5  $\mu\text{m}$ ) in a trade-off of lateral localization precision and can, in theory, achieve isometric resolution. Other approaches such as opposing objective lenses (4Pi arrangement) [11] or interferometric SMLM [12] can achieve a sub-10 nm axial resolution, but require a complex optical system design. To image samples thicker than 5  $\mu\text{m}$ ,  $Z$ -scanning is needed, which is typically achieved by physically moving either the sample or the objective axially with a piezoelectric stage. Alternatively, light-sheet illumination with Bessel beams can be used for structured sample illumination, increasing the axial resolution [13], but requiring a separate objective lens placed in close proximity to the sample [13, 14].

Furthermore, biplane imaging with 50:50 beam splitters or image splitting prisms can be used to separate the detection path into multiple planes [15–17], thus enabling a simultaneous volume acquisition in exchange for signal-to-noise ratio. However, when imaging deeper into the sample, aberrations induced by the optical system distort the PSF and ultimately diminish the localization precision. This is a particular problem for high NA oil immersion objectives because of the refractive index mismatch between the imaging medium and immersion oil. Fortunately, these intrinsic aberrations, together with inhomogeneities in the refractive index of the biological sample volume, can be partially corrected by the use of adaptive optics [18].

To appropriately sample complex cellular structures, 3D-SMLM experiments in their extreme can run for long durations ranging from a few hours [10] to multiple days [19], presenting a significant challenge in lateral and axial drift correction. Lateral drift is typically corrected in post-processing by tracking fiducial markers. On the other hand, axial drift correction requires an active feedback loop which is commonly achieved by measuring the lateral displacement of an infrared laser set up in total internal reflection [20], computing the three dimensional correlation between a previously recorded brightfield  $Z$ -stack in a separate imaging channel and a live brightfield image [21] or by tracking fiducial markers in three dimensions [22].

To perform a precise and continuous axial drift correction while imaging multiple  $Z$ -slices of the cell volume, commercially available complex  $Z$ -stabilization systems

using movable offset lenses are needed to compensate for the changing distance between the objective lens and the coverslip. In the alternative approach, termed remote focusing, one changes the focus without moving either the objective or the coverslip. The approach involves shifting the image plane by optical defocusing using an adaptive optical element. This can be achieved at a few kHz rates by using a deformable mirror or an electrically tunable lens [23] and does not require movement of sample or objective [24].

Here, we demonstrate a combined application of AO in super-resolution microscopy by fusing point-spread function engineering, aberration correction and simultaneous rapid remote focusing. It enables us to record  $Z$ -stacks of whole COS-7 cells without moving the sample and keeping it axially stabilized for extended periods of time (here up to 2.5 h). Fast remote focusing also allows us to change the image planes frequently (maximum frequency of 100 Hz), thus homogeneously distributing the effect of bleaching in all the planes by revisiting the same imaging plane multiple times. Finally, we perform multiplane super-resolution microscopy by processing the data with different modalities by using SOFI, 2D SMLM and astigmatism-based 3D SMLM for further increased depth sampling with self-blinking fluorescent probes.

## 2 Materials and methods

### 2.1 Setup

Imaging was performed on a custom-built microscope [25] (Figure 1(a)). 100 mW 488 nm (Sapphire, Coherent) and 100 mW 561 nm (Excelsior, Spectra Physics) continuous lasers were used for excitation. Laser beams were combined using a dichroic mirror (T495lpxr, Chroma) and passed through an acousto-optic tunable filter (AOTFnC-VIS-TN, AA Opto Electronic), which is used to modulate the power of both lasers independently. Beams were passed through an achromatic  $\lambda/4$  plate (AQWP05M-600, Thorlabs), expanded with a 10 $\times$  telescope ( $d = 12$  mm) and focused with a  $f = 300$  mm lens into the back focal plane of the objective mounted on an inverted optical microscope (IX71, Olympus). 100 $\times$  oil-immersion objective (UApo N  $\times$  100, Olympus) with a numerical aperture of 1.49 was used for imaging. Fluorescence signal collected by the objective was filtered using a combination of a quad-line dichroic mirror (R405/488/561/635, Chroma) and two emission filters: quad-line (446/523/600/677 HC Quadband, Semrock) and band-pass (596/83, Chroma). Fluorescence is then passed into the adaptive optics add-on (MicAO 3DSR, Imagine Optic) where the back focal plane of the objective is conjugated to a deformable mirror (MIRA0 52e, Imagine Optic). A flip mirror is used to deflect the light either to a Shack-Hartmann wave-front sensor (HASO3, Imagine Optic) or to an EMCCD camera (iXon DU-897, Andor). The camera was water-cooled with a custom-built water-cooling system to prevent vibrations from the camera fan. The motorized XYZ stage (MS-2000, ASI) was used for coarse positioning of the sample,

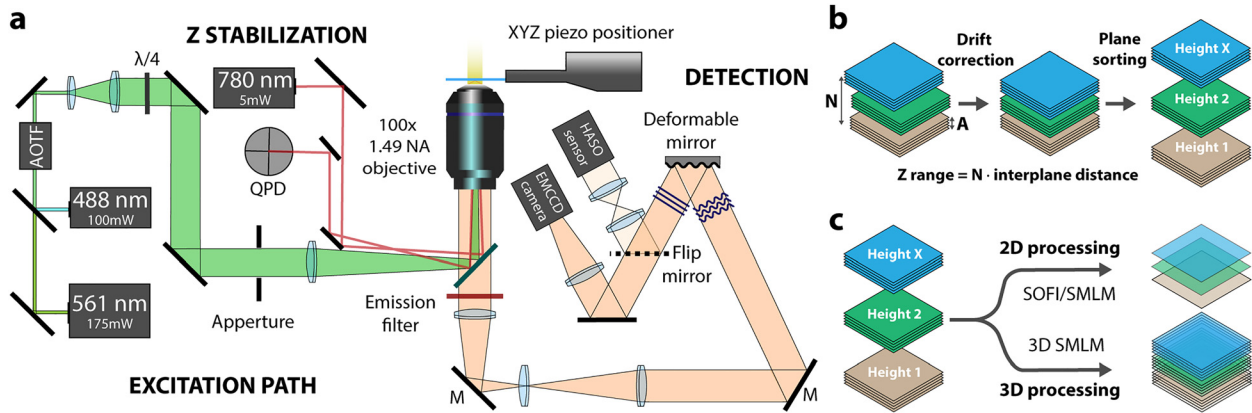


**Figure 1:** Schematics of the optical setup and image processing pipeline.

(a) Sample excitation was achieved by two continuous laser sources with independently modulated power by acousto-optic tunable filter. Laser beams were then expanded with a telescope and focused by a lens into the back focal plane of the  $100\times$   $NA = 1.49$  oil immersion objective to achieve a widefield illumination of the sample. Fluorescence light was collected by the same objective and filtered using a combination of a dichroic mirror and two emission filters. The light is then passed through MicAO 3DSR adaptive optics setup which consists of a deformable mirror and a wavefront sensor. Light is then detected either by a wavefront sensor, which is used for a calibration of AO system or a water-cooled EMCCD camera with a back-projected pixel size of 105 nm. Total internal reflection of an infrared laser is used to axially stabilize the sample which is precisely positioned by the XYZ piezo stage thus eliminating the axial drift. (b) 3D image stacks were recorded by shifting the height using a deformable mirror every  $A$  number of frames in order to homogeneously distribute bleaching in all the  $N$  planes. Fluorescent beads immobilized on a coverslip were imaged every  $A$  number of frames with a 488 nm laser line and then used for lateral drift correction (SI drift correction). For final processing image stacks were sorted based on focus values applied for each frame. (c) Substacks were processed by using SOFI and SMLM routines published previously as described in Section 2.

with a XYZ piezo stage (LPS Series, Mad City lab) for fine XYZ positioning, including axial sample stabilization. For the home-built Z-stabilization system, a collimated beam from a 785 nm laser diode (Thorlabs, LPS-785-FC) was focused on the back focal plane of the objective far from the optical axis in order to undergo total-internal reflection from the sample-coverslip interface [20]. IR reflection was filtered with a band-pass filter (FL780-10, Chroma) and deflected on a quadrant photo diode (QPD, Pacific Silicon QP50-6SD2). The QPD signal is used in the PID controller implemented in LabView, which forms a closed-loop system with the piezo stage and ensures the Z-stabilization of the sample. The whole setup, including the deformable mirror was controlled with a custom LabView program.

## 2.2 Sample preparation

Cells were cultured in DMEM high glucose without phenol red medium (Gibco, Thermo Fisher Scientific), containing 10% fetal bovine serum (Gibco, Thermo Fisher Scientific), 1% penicillin-streptomycin (Gibco, Thermo Fisher Scientific) and 4 mM L-glutamine (Gibco, Thermo Fisher Scientific) at 37 °C and 5%  $CO_2$ . Cells were detached from a flask with TrypLE (Gibco, Thermo Fisher Scientific) and seeded on 25 mm coverslips coated with fibronectin. Cells were grown overnight (12–16 h) before fixation in 6-well plates. During fixation, coverslips were incubated for 90 s in a prewarmed microtubule extraction buffer, consisting of 80 mM PIPES, 7 mM  $MgCl_2$ , 1 mM EDTA, 150 mM NaCl and 5 mM D-glucose with a pH adjusted to 6.8 using KOH with 0.3% (v/v) Triton X-100 (AppliChem) and 0.25% (v/v) EM-grade glutaraldehyde (Electron Microscopy Sciences). The solution was exchanged to prewarmed 4% paraformaldehyde dissolved in PBS (pH = 7.4) and

samples were incubated for 10 min at room temperature. Afterward, samples were washed three times for 5 min with PBS on an orbital shaker. Cells were kept for 5 min with a freshly prepared 10 mM  $NaBH_4$  solution in PBS on an orbital shaker in order to reduce background fluorescence. This step was followed by a rinse in PBS, and two washes of 10 min in PBS on an orbital shaker. Samples were then additionally permeabilized to ensure antibody penetration with 0.1% (v/v) Triton X-100 in PBS (pH = 7.4) on an orbital shaker followed by an additional wash with PBS. Finally, samples were blocked with freshly prepared blocking buffer consisting of 2% (w/v) BSA, 10 mM glycine, 50 mM ammonium chloride  $NH_4Cl$  in PBS (pH = 7.4) for 60 min at room temperature or stored overnight at 4 °C for further staining. All chemicals were bought from Sigma Aldrich unless stated differently. After blocking, samples were incubated with 2% (v/v) primary anti-tubulin antibody (clone B-5-1-2, Sigma-Aldrich) in blocking buffer for 60 min at room temperature. Samples were washed with blocking buffer thrice for 5 min on orbital shaker. Coverslips were incubated with 2% (v/v) secondary donkey anti-mouse-Abberior FLIP-565 antibody, which was labeled as described previously [26]. Samples were kept in blocking buffer for 60 min and washed thrice for 5 min on orbital shaker. Samples were incubated for 10 min in 2% (w/v) PFA in PBS (pH = 7.4) as a post-fixation step followed by three 5 min washes with PBS on an orbital shaker. After staining, samples were incubated with a 1% fluorescent (Ex. 505/Em. 515 nm) 175 nm diameter beads solution (PS-Speck™, Invitrogen) for 10 min and then washed with PBS. Finally, PBS (pH = 7.4) was saturated with argon by passing the gas through the solution for at least 1 h, thus reducing the  $O_2$  concentration to  $\approx 0.01$  ppm in order to prevent photobleaching of the fluorophore. The degassed buffer was subsequently used for imaging in a closed imaging chamber.

### 2.3 *In vitro* imaging and calibration routines

The AO system was pre-calibrated before starting imaging experiments using a routine provided by the manufacturer (Image Optic). For the calibration, we imaged an isolated 1  $\mu\text{m}$  bead immobilized on a surface while operating the DM in a closed-loop mode with the Shack-Hartmann wavefront sensor to establish an interaction matrix, which was further used for routine image-based indirect calibration. Before acquiring each Z-stack, the PSF of an isolated 175 nm fluorescent bead immobilized on a surface was imaged with the 488 nm laser and it was used to correct aberrations in each field-of-view. MicAO software (Image Optic) was used with an integrated 3N algorithm [27] which exploits a maximum contrast as an optimization metric to correct for the wavefront distortions by finding the amplitudes of selected first 15 Zernike modes. After correction, the mirror shape was used with a custom-written LabView program controlling the microscope. For each mirror shape a z-stack of the beads in agarose gel was recorded to calibrate the axial shifts induced by the DM (SI Figure 2). In order to correct the lateral field-of-view (FOV) distortion, the beads immobilized on the surface were imaged with different focus values added with a DM (SI Figure 3). For Abberior FLIP-565 imaging a 561 nm laser was used for excitation with a power ranging from 300  $\text{W}/\text{cm}^2$  for regular imaging to 1400  $\text{W}/\text{cm}^2$  for astigmatism-based imaging. Exposure time in all experiments was 50 ms, using an EM gain of 150. The Z-stacks with remote DM focusing were typically recorded within the 10  $\mu\text{m}$  range, due to the thickness of the cells by adding a specific amount of defocus on top of the mirror shape. The Z-stacks were recorded by specifying the number of equally spaced planes ( $N$ ) within the selected range. The number of frames ( $A$ ) and the number of repeats ( $B$ ) for the whole axial range were specified, resulting in the total number of  $N \cdot A \cdot B$  frames per volume. After each  $A$  frames-long sequence, the DM was set to 0 nm position and the image of beads was taken with 488 nm laser for a lateral drift correction in post-processing (Figure 1(b)). For astigmatic-based 3D SMLM imaging, 60 nm root-mean-square (RMS) of astigmatism was added using the DM. The RMS value in nm describes the amplitude of the Zernike coefficient, which is the total amount of RMS displacement of the mirror with respect to a flat surface. Furthermore, the 60 nm RMS of 3rd order spherical aberration per 10  $\mu\text{m}$  of depth was linearly added in order to compensate for spherical aberration resulting from the refractive index mismatch between water and the objective's immersion oil based on the calibration [28] provided by a manufacturer. Finally, the exact values of the focus applied on the DM were saved to a separate file for image stack sorting.

### 2.4 Image processing

Acquired image stacks were sorted based on the input defocus values and drift-corrected based on the acquired bead stacks (SI Figure 1). Stacks were processed based on the acquisition mode used for imaging. Z-stacks without added astigmatism were processed with a 2D SOFI algorithm implemented in Matlab based on the previous work [29] or with SMLM software Thunderstorm [30] by using the integrated Gaussian PSF model and weighted least-squares fitting method. 2D SMLM stacks were filtered by removing localizations with lateral uncertainty  $>45$  nm and sigma values  $<80$  or  $>140$  nm. Stacks with 60 nm RMS of added astigmatism were also processed with the Thunderstorm 3D localization routine. For final figures, localizations were filtered by removing localizations with lateral uncertainty  $>45$  nm and axial

uncertainty  $>100$  nm. SOFI images were deconvolved with a Lucy-Richardson deconvolution algorithm with 25 iterations using Gaussian PSF model. For data with added astigmatism, an elliptical Gaussian model was used with weighted least square fitting method. The intrinsic axial shift between different planes was corrected by estimating the axial shift for each mirror shape by using a bead stack recorded with the piezo in agarose as a reference (SI Figure 2) while the lateral FOV distortion was corrected for each height plane as described in SI Figure 3. Final SMLM images were also rendered in Thunderstorm software by using the averaged shifted histogram method with 10.5 nm pixel size. Localization precision was estimated in Thunderstorm software as well by using a 12.26 photoelectrons per count conversion factor calculated from the experimental photon transfer curve.

## 3 Results

In order to demonstrate the advantages of our approach, we labeled microtubules in fixed COS-7 cells with a self-blinking Abberior FLIP-565 dye which does not need a complex imaging buffer for blinking and was used previously for SOFI [26] and SMLM [31, 32]. A custom-built widefield microscope equipped with a high NA oil immersion objective and an adaptive optics add-on was used for imaging as shown in Figure 1(a) and further explained in Section 2. We were able to record Z-stacks by changing the focus remotely i.e. by adding or subtracting a specific amount of Zernike defocus mode ( $Z_2^0$ ) via the deformable mirror, thus keeping the sample stationary by a closed-loop Z-stabilization system at all times. The stacks of blinking emitters were recorded in a predefined Z-range by shifting the focus every  $A$  (200–500) frames (Figure 1(b)). An image of the beads immobilized on the coverslip was taken after each such subsequence in order to estimate the lateral drift and correct it in post-processing (SI Figure 1).

The drift-corrected stacks were then processed with three different super resolution processing algorithms (Figure 1(c)) in order to show the versatility of our method.

Z-stacks were first processed with the versatile SOFI approach [4] to demonstrate the multiplane high-order SOFI imaging capability (Figure 2). Since the AO does not allow the acquisition of several planes simultaneously, SOFI can only be computed along the lateral dimensions, plane by plane, resulting in a 2.5D volume. In comparison to simultaneous volume recording in a 3D SOFI approach with an image-splitting component [16, 33], the AO element allowed to achieve similar lateral resolution for deconvolved 4th order SOFI images ( $75 \pm 6$  nm compared to  $78 \pm 7$  nm) within the higher axial depth in an exchange of longer imaging times (SI Figure 4). The stack consisted of 20 planes spaced approx. 500 nm apart with 6000 frames in total recorded for each plane. The distances between

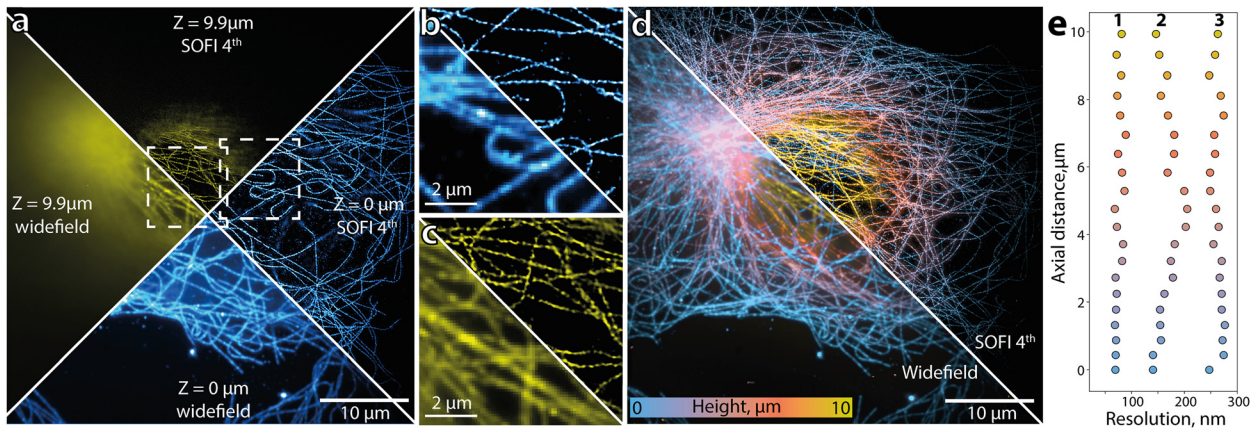


**Figure 2:** Sequential-plane imaging with SOFI.

(a) Images of tubulin of a COS-7 cell immunostained with Abberior FLIP-565 self-blinking dye acquired from different heights of 0  $\mu\text{m}$  (blue) and 9.9  $\mu\text{m}$  (yellow). A comparison of a widefield and SOFI 4th order images recorded at 0  $\mu\text{m}$  (b) and 9.9  $\mu\text{m}$  (c) indicates a clear contrast and resolution improvement provided by SOFI. (d) An overlay of 20 planes spaced with approx. 500 nm axial distance. (e) Lateral resolution dependency on height for different SOFI orders (1 – SOFI 4th, 2 – SOFI 2nd, 3 – widefield).

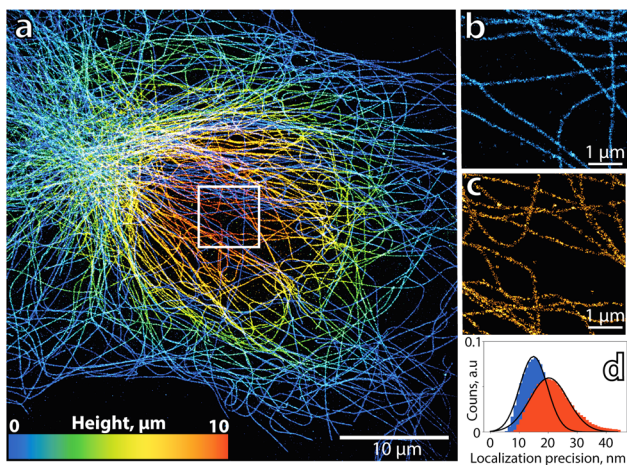


**Figure 3:** Multiplane single-molecule localization microscopy.

(a) A height coded render of 20 resolved planes spaced 500 nm apart. The same dataset as in Figure 2 was processed. (b–c) Zoom-ins from the bottom (b) and top (c) planes. (d) Localization precision histogram showing a localization precision difference of 5.3 nm in the 10  $\mu\text{m}$  axial range.

planes were estimated via additional calibrations using a bead stack recorded with a piezo actuator (SI Figure 2) as a reference. The stack was recorded by shifting the focus after 200 frames (10 s) in order to keep the bleaching effect homogenous within the whole volume (SI Figure 5) with an average bleaching lifetime of  $54 \pm 4$  min due to a low laser power used ( $300 \text{ W}/\text{cm}^2$ ). We found that continuous tubulin structures were resolved in 4th order SOFI images within the whole 10  $\mu\text{m}$  axial range (Figure 2(b)) and without an observable difference in estimated image resolution (Figure 2(d) and (e)). To further demonstrate the versatility of our approach, the same image stack as in

Figure 2 was processed with a SMLM approach (Figure 3) by localizing emitters with a standard routine (see Section 2 for more details). This allowed us to quantify the localization precision and density at different planes (SI Figure 7). Furthermore, we observed a decrease (5.3 nm) of localization precision when comparing the localization precision histograms of the bottom (0  $\mu\text{m}$ ) and top planes (9.9  $\mu\text{m}$ ) (Figure 3(d)). This decrease is likely due to wavefront distortions introduced by the sample causing additional aberrations and could be in principle corrected by using state-of-the-art *in-situ* image-based online aberration estimation algorithms [34, 35] and correcting each Z-plane of the stack independently to gain maximum performance. Finally, samples were also imaged by adding 60 nm RMS astigmatism at  $0^\circ$  using the same DM to perform an astigmatism-based 3D SMLM with an AO. The calibration curves of the astigmatic PSF using 175 nm diameter beads were recorded at the bottom plane (SI Figure 6) and then used with a standard 3D SMLM routine. 11 slices with an axial distance of approx. 1  $\mu\text{m}$  apart were imaged by changing the height in 300 frame intervals and recording 15,000 frames for each Z-slice (165,000 frames in total;  $\approx 2 \text{ h } 20 \text{ min}$ ). The final 3D stack (Figure 4(a), SI Figure 9, SI Video 1) demonstrates the ability to perform astigmatism-based 3D SMLM within a 10  $\mu\text{m}$  axial depth by using AO remote focusing. The height color-coded Z-slices near the bottom (0–0.8  $\mu\text{m}$ ) and top (8.4–9.2  $\mu\text{m}$ ) of the stacks displays the axial dynamic range. The 1  $\mu\text{m}$  interplane distance used for a particular 3D stack resulted in a reduced number of localizations between the planes and suboptimal Z-sampling, which can be improved by using smaller interplane distances (SI Figure 8(a)) at the cost of lateral sampling due

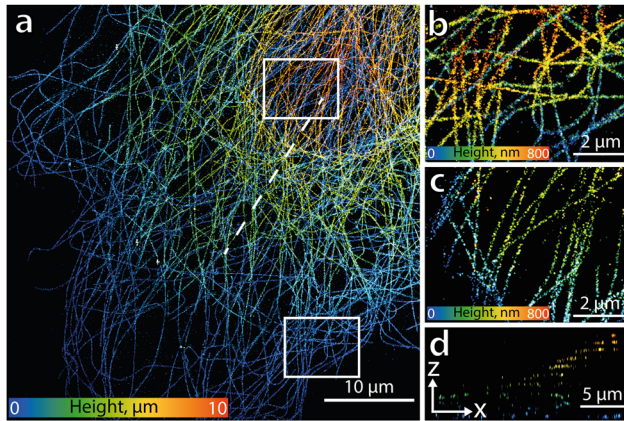


**Figure 4:** Multiplane astigmatism-based single-molecule localization microscopy.

(a) A height coded render of tubulin in a COS-7 cell immunostained with Abberior FLIP-565 self-blinking dye imaged by adding 60 nm RMS of astigmatism. (b–c) Zoom-ins from the bottom (b) and top (c) planes of the full image stack (d) A slice marked in (a) with a dashed line showing the axial profile of the whole volume consisting of 10 sub-volumes spaced with 1  $\mu\text{m}$  distance.

to bleaching effects. Furthermore, lateral localization precision decreased from 29 to 38 nm per 8  $\mu\text{m}$  of depth (SI Figure 8(b)), while the axial localization precision of 130 nm stayed similar through the depth range (SI Figure 8(c)). It is important to note that our choice of an Abberior FLIP-565 self-blinking dye was motivated by its flexibility for different super-resolution modalities, and this dye is suboptimal for 3D SMLM experiments in terms of photon yield and average ON/OFF ratio [36]. Localization precision may be improved by using brighter fluorescent probes such as Alexa647 under STORM conditions [37] allowing one to reach sub 20 nm lateral and axial localization precisions.

## 4 Conclusion

We demonstrated a proof-of-principle application of adaptive optics for multimode 3D super-resolution microscopy imaging over a 10  $\mu\text{m}$  axial range with a deformable mirror for remote focusing combined with aberration correction for 2.5D SOFI and astigmatism-based 3D SMLM achieving sub-diffractional resolution across all modalities. We have expanded the previously demonstrated astigmatism-based 3D SMLM [9, 18] using a deformable mirror to higher axial range by applying the focus mode in order to image multiple planes. A high axial range is important to visualize various biological structures such as cortical neurons [38]. By exploiting the AO advantages for deep imaging with high-NA oil-immersion objectives, described in detail recently [18], we

exploited the remote focus functionality to accommodate the ability to capture the whole cellular volume without moving the sample. Our approach can be easily applied to existing setups equipped with DMs, simplifying acquisition and Z-stabilization of high-resolution 3D image stacks via multiple super-resolution microscopy modalities requiring long acquisition times such as DNA-PAINT [39] and Exchange-PAINT [40], further automatizing the imaging process. Compared to biplane or multifocal SMLM imaging approaches using image splitting elements [17], the emission signal is not divided, thus preserving the signal-to-noise ratio and remaining flexible in terms of interplane distance and imaging depth, which can be further extended to perform SMLM in tissues [34, 41]. Furthermore, the image-based wavefront calibration procedure can also be improved to account for distortions further away from the image center [18] by using global optimization techniques [34], enabling correction of sample-induced aberrations through the whole available field-of-view. From the data analysis standpoint, novel deep-learning approaches can further refine our technique by improving the accuracy of localizations [42] or reducing the number of frames needed for image reconstruction [43]. We believe that our study will foster the use of adaptive optics in modern fluorescence microscopy for biological applications requiring high-throughput and high-resolution imaging.

**Acknowledgements:** V.N. and A.R. acknowledge the Max-Planck EPFL Center for Molecular Nanoscience and Technology as well as NCCR in Biomaterials. V.N. is grateful for Flavien Colaço for the help in Labview programming and Audrius Jasaitis from Imagine Optic for technical assistance with the AO setup. A.R. and A.D. acknowledge the support of the EPFL Open Science fund.

**Author contributions:** All the authors have accepted responsibility for the entire content of this submitted manuscript and approved submission.

**Research funding:** This research was funded by Schweizerischer Nationalfonds zur Förderung der Wissenschaftlichen Forschung.

**Conflict of interest statement:** The authors declare no conflicts of interest regarding this article.

## References

- [1] S. J. Sahl, S. W. Hell, and S. Jakobs, “Fluorescence nanoscopy in cell biology,” *Nat. Publ. Gr.*, vol. 18, 2017, <https://doi.org/10.1038/nrm.2017.71>.
- [2] M. J. Rust, M. Bates, and X. Zhuang, “Sub-diffraction-limit imaging by stochastic optical reconstruction microscopy (STORM),” *Nat. Methods*, vol. 3, pp. 793–796, 2006.

- [3] E. Betzig, G. H. Patterson, R. Sougrat, et al., “Imaging intracellular fluorescent proteins at nanometer resolution,” *Science (80-)*, vol. 313, pp. 1642–1645, 2006.
- [4] T. Dertinger, R. Colyer, G. Iyer, S. Weiss, and J. Enderlein, “Fast, background-free, 3D super-resolution optical fluctuation imaging (SOFI),” *Proc. Natl. Acad. Sci. U. S. A.*, vol. 106, pp. 22287–92, 2009.
- [5] R. J. Marsh, K. Pfisterer, P. Bennett, et al., “Artifact-free high-density localization microscopy analysis,” *Nat. Methods*, vol. 15, pp. 689–692, 2018.
- [6] S. Geissbuehler, C. Dellagiocoma, and T. Lasser, “Comparison between SOFI and STORM,” *Biomed. Opt. Express*, vol. 2, p. 408, 2011.
- [7] L. Schermelleh, A. Ferrand, T. Huser, et al., “Super-resolution microscopy demystified,” *Nat. Cell Biol.*, vol. 21, pp. 72–84, 2019.
- [8] B. Huang, W. Wang, M. Bates, and X. Zhuang, “Three-dimensional super-resolution imaging by stochastic optical reconstruction microscopy,” *Science (80-)*, vol. 319, pp. 810–813, 2008.
- [9] I. Izeddin, M. El Beheiry, J. Andilla, D. Ciepielewski, X. Darzacq, and M. Dahan, “PSF shaping using adaptive optics for three-dimensional single-molecule super-resolution imaging and tracking,” *Opt. Express*, vol. 20, p. 4957, 2012.
- [10] A. Aristov, B. Lelandais, E. Rensen, and C. Zimmer, “ZOLA-3D allows flexible 3D localization microscopy over an adjustable axial range,” *Nat. Commun.*, vol. 9, pp. 1–8, 2018.
- [11] U. Böhm, S. W. Hell, and R. Schmidt, “4Pi-RESOLFT nanoscopy,” *Nat. Commun.*, vol. 7, pp. 1–8, 2016.
- [12] G. Shtengel, J. A. Galbraith, C. G. Galbraith, et al., “Interferometric fluorescent super-resolution microscopy resolves 3D cellular ultrastructure,” *Proc. Natl. Acad. Sci. U. S. A.*, vol. 106, pp. 3125–3130, 2009.
- [13] T. A. Planchon, L. Gao, D. E. Milkie, et al., “Rapid three-dimensional isotropic imaging of living cells using Bessel beam plane illumination,” *Nat. Methods*, vol. 8, pp. 417–423, 2011.
- [14] C. H. Lu, W. C. Tang, Y. T. Liu, et al., “Lightsheet localization microscopy enables fast, large-scale, and three-dimensional super-resolution imaging,” *Commun. Biol.*, vol. 2, pp. 1–10, 2019.
- [15] S. Abrahamsson, J. Chen, B. Hajj, et al., “Fast multicolor 3D imaging using aberration-corrected multifocus microscopy,” *Nat. Methods*, vol. 10, pp. 60–63, 2013.
- [16] A. Descloux, K. S. Grubb, E. Bostan, et al., “Combined multiplane phase retrieval and super-resolution optical fluctuation imaging for 4D cell microscopy,” *Nat. Photonics*, vol. 12, pp. 165–172, 2018.
- [17] L. Oudjedi, J.-B. Fiche, S. Abrahamsson, et al., “Astigmatic multifocus microscopy enables deep 3D super-resolved imaging,” *Biomed. Opt. Express*, vol. 7, p. 2163, 2016.
- [18] M. Siemons, B. M. C. Cloin, D. M. Salas, W. Nijenhuis, E. A. Katrukha, and L. C. Kapitein, “Comparing strategies for deep astigmatism-based single-molecule localization microscopy,” *Biomed. Opt. Express*, vol. 11, p. 735, 2020.
- [19] D. P. Hoffman, G. Shtengel, C. S. Xu, et al., “Correlative three-dimensional super-resolution and block-face electron microscopy of whole vitreously frozen cells,” *Science (80-)*, vol. 367, 2020.
- [20] P. Annibale, M. Scarselli, M. Greco, and A. Radenovic, “Identification of the factors affecting co-localization precision for quantitative multicolor localization microscopy,” *Opt. Nanoscopy*, vol. 1, pp. 1–13, 2012.
- [21] R. Mcgorty, D. Kamiyama, and B. Huang, “Active microscope stabilization in three dimensions using image correlation,” *Opt. Nanoscopy*, vol. 2, 2013, <https://doi.org/10.1186/2192-2853-2-3>.
- [22] S. Coelho, J. Baek, J. Walsh, J. J. Gooding, and K. Gaus, “3D active stabilization for single-molecule imaging,” *Nat. Protoc.*, vol. 16, pp. 497–515, 2021.
- [23] M. Bathe-Peters, P. Annibale, and M. J. Lohse, “All-optical microscope autofocus based on an electrically tunable lens and a totally internally reflected IR laser,” *Opt. Express*, vol. 26, p. 2359, 2018.
- [24] M. Žurauskas, O. Barnstedt, M. Frade-Rodriguez, S. Waddell, and M. J. Booth, “Rapid adaptive remote focusing microscope for sensing of volumetric neural activity,” *Biomed. Opt. Express*, vol. 8, p. 4369, 2017.
- [25] H. Deschout, T. Lukes, A. Sharipov, et al., “Complementarity of PALM and SOFI for super-resolution live-cell imaging of focal adhesions,” *Nat. Commun.*, vol. 7, p. 13693, 2016.
- [26] K. Grubb, T. Lukes, T. Lasser, and A. Radenovic, “Self-blinking dyes unlock high-order and multiplane super-resolution optical fluctuation imaging,” *ACS Nano*, vol. 14, pp. 9156–9165, 2020.
- [27] M. J. Booth, M. A. A. Neil, R. Juškaitis, and T. Wilson, “Adaptive aberration correction in a confocal microscope,” *Proc. Natl. Acad. Sci. U. S. A.*, vol. 99, pp. 5788–5792, 2002.
- [28] V. Fraissier, G. Clouvel, A. Jasaitis, A. Dimitrov, T. Piolot, and J. Salameo, “Adaptive optics in spinning disk microscopy: improved contrast and brightness by a simple and fast method,” *J. Microsc.*, vol. 259, pp. 219–227, 2015.
- [29] S. Geissbuehler, N. L. Bocchio, C. Dellagiocoma, C. Berclaz, M. Leutenegger, and T. Lasser, “Mapping molecular statistics with balanced super-resolution optical fluctuation imaging (bSOFI),” *Opt. Nanoscopy*, vol. 1, pp. 1–7, 2012.
- [30] M. Ovesný, P. Křížek, J. Borkovec, et al., “ThunderSTORM: A comprehensive ImageJ plug-in for PALM and STORM data analysis and super-resolution imaging,” *Bioinformatics*, vol. 30, pp. 2389–90, 2014.
- [31] M. Bossi, J. Fölling, V. N. Belov, et al., “Multicolor far-field fluorescence nanoscopy through isolated detection of distinct molecular species,” *Nano Lett.*, vol. 8, pp. 2463–2468, 2008.
- [32] R. Galland, G. Greci, A. Aravind, V. Viasnoff, V. Studer, and J.-B. Sibarita, “3D high-and super-resolution imaging using single-objective SPIM,” *Nat. Methods*, vol. 12, pp. 641–644, 2015.
- [33] S. Geissbuehler, A. Sharipov, A. Godinat, et al., “Live-cell multiplane three-dimensional super-resolution optical fluctuation imaging,” *Nat. Commun.*, vol. 5, pp. 1–7, 2014.
- [34] M. E. Siemons, N. A. K. Hanemaaijer, M. H. P. Kole, and L. C. Kapitein, “REALM: AO-based localization microscopy deep in complex tissue,” *bioRxiv*, 2020, <https://doi.org/10.1101/2020.06.12.147884>.
- [35] D. Saha, U. Schmidt, Q. Zhang, et al., “Practical sensorless aberration estimation for 3D microscopy with deep learning,” *Opt. Express*, vol. 28, pp. 29044–29053, 2020.
- [36] G. T. Dempsey, J. C. Vaughan, K. H. Chen, M. Bates, and X. Zhuang, “Evaluation of fluorophores for optimal performance in localization-based super-resolution imaging,” *Anal. Nat. methods*, vol. 8, 2011, <https://doi.org/10.1038/nmeth.1768>.

- [37] N. Olivier, D. Keller, P. Gönczy, and S. Manley, "Resolution doubling in 3D-STORM imaging through improved buffers," *PLoS One*, vol. 8, p. e69004, 2013.
- [38] B. E. Urban, L. Xiao, S. Chen, et al., "In vivo superresolution imaging of neuronal structure in the mouse brain," *IEEE Trans. Biomed. Eng.*, vol. 65, pp. 232–238, 2018.
- [39] J. Schnitzbauer, M. T. Strauss, T. Schlichthaerle, F. Schueder, and R. Jungmann, "Super-resolution microscopy with DNA-PAINT," *Nat. Protoc.*, vol. 12, pp. 1198–1228, 2017.
- [40] R. Jungmann, M. S. Avendaño, J. B. Woehrstein, M. Dai, W. M. Shih, and P. Yin, "Multiplexed 3D cellular super-resolution imaging with DNA-PAINT and Exchange-PAINT," *Nat. Methods*, vol. 11, pp. 313–318, 2014.
- [41] J. Kim, M. Wojcik, Y. Wang, et al., "Oblique-plane single-molecule localization microscopy for tissues and small intact animals," *Nat. Methods*, vol. 16, pp. 853–857, 2019.
- [42] A. Speiser, L.-R. Müller, U. Matti, et al., "Deep learning enables fast and dense single-molecule localization with high accuracy," *bioRxiv*, 2020, <https://doi.org/10.1101/2020.10.26.355164>.
- [43] W. Ouyang, A. Aristov, M. Lelek, X. Hao, and C. Zimmer, "Deep learning massively accelerates super-resolution localization microscopy," *Nat. Biotechnol.*, vol. 36, pp. 460–468, 2018.

---

**Supplementary Material:** The online version of this article offers supplementary material (<https://doi.org/10.1515/nanoph-2021-0108>).